Probing the Electrochemical Li Insertion–Extraction Mechanism in Sputtered LiNi0.5Mn1.5O4 Thin Film Cathode for Li-Ion Microbattery

Ankush Bhatia, Clement Leviel, Maxime Hallot, Jean Pierre Pereira-Ramos, Christophe Lethien, Pascal Roussel, Rita Baddour-Hadjean

Probing the Electrochemical Li Insertion-Extraction Mechanism in Sputtered $LiNi_{0.5}Mn_{1.5}O_4$ Thin Film Cathode for Li-ion Microbattery

Ankush Bhatia, Clement Leviel, Maxime Hallot, Jean-Pierre Pereira Ramos, Christophe Lethien, Pascal Roussel*, and Rita Baddour-Hadjean'**

A. Bhatia, J. P. Pereira-Ramos, R. Baddour-Hadjean
Institut de Chimie et des Matériaux Paris-Est (ICMPE), UMR 7182 CNRS-UPEC, 2 rue Henri Dunant, F-94320 Thiais, France
E-mail: rita.baddour-hadjean@cnrs.fr

C. Leviel, P. Roussel
Université de Lille, Centrale Lille, Université d'Artois, Unité de Catalyse et de Chimie du Solide (UCCS), UMR 8181 CNRS, F-59000 Lille, France
E-mail: pascal.roussel@univ-lille.fr

C. Leviel, M. Hallot, C. Lethien
Univ. Lille, CNRS, Univ. Polytechnique Hauts-de-France, UMR 8520 - IEMN - Institut d'Electronique de Microélectronique et de Nanotechnologie, F-59000 Lille, France
E-mail: christophe.lethien@univ-lille.fr

C. Leviel, M. Hallot, C. Lethien
Réseau sur le Stockage Electrochimique de l'Energie (RS2E), CNRS FR 3459, 33 rue Saint Leu, 80039 Amiens Cedex, France

C. Lethien
Institut Universitaire de France, 75005 Paris, France

Keywords: Li-ion micro-battery, $LiNi_{0.5}Mn_{1.5}O_4$ thin film, high voltage spinel, cathode, Raman spectroscopy

Due to its great theoretical capacity (147 $mAh \cdot g^{-1}$) and high operating potential (4.7 V vs Li^+/Li), Co-free spinel $LiNi_{0.5}Mn_{1.5}O_4$ (LNMO) is one of the most promising thin film cathode allowing designing Li-ion micro-batteries with a high specific energy. In this work, the Li extraction-insertion mechanism in sputtered LNMO thin films is investigated by X-ray diffraction and Raman spectroscopy during the first electrochemical cycle. A one-step phase transition involving two cubic phases is revealed, consisting in a wide solid solution region ($0.4 \leq x \leq 1$ in Li_xNMO) and a narrow biphasic domain ($0 < x \leq 0.3$). Remarkably, significant variations are observed in the Raman spectra, which are linked to the activity of the Ni redox system at 4.7 V. We demonstrate that an appropriate analysis of the bands corresponding to pure Ni-O stretching modes leads to an accurate estimation of the electrode states of charge and discharge, which opens the way for a reliable quantification of the self-discharge phenomenon. The mechanism of Li extraction insertion here pictured for the first time for LNMO thin layers is consistent with their disordered nature and accounts for their good electrochemical performance.

1. Introduction

Tremendous progress in the miniaturization of electronic components has been achieved over the past three decades. This phenomenon is nowadays further emphasized by the emergence of new networks of miniaturized nomadic or stand-alone products in civil and military domains, integrating the so-called Internet of Things (IoT). These devices require on-board energy resources for measurement, processing and communication of information within a network. In this context of miniaturization, thin-film Li-ion microbatteries are a favorite option due to their superior energy density, but there is still a need to meet the high energy and power demands of IoT applications. The judicious choice of cathode materials in thin film configuration is thus an essential step in the development of Li-ion microbatteries.

Chemical vapor deposition and sputtering have been the most frequently used techniques to synthesize mostly $LiCoO_2$ and $LiMn_2O_4$ thin films, with electrode potentials of 3.8 and 4.1 V vs Li/Li^+, respectively.[1,2] The partial replacement of manganese in $LiMn_2O_4$ with various transition metals is known to endow this compound with the ability to deliver a substantial capacity at a high voltage near 4.5 V.[3] $LiNi_{0.5}Mn_{1.5}O_4$ (LNMO) is the substituted spinel exhibiting the best electrochemical properties relying entirely on the nickel redox system (Ni^{2+} being oxidized in Ni^{3+} and Ni^{4+}) at a high working potential of about 4.7 V vs Li/Li^+. Furthermore, the substitution of 25% of manganese by nickel allows having manganese only in the +4 oxidation state in the structure, then preventing detrimental effects such as Jahn-

Teller distortion as well as disproportionation of Mn^{3+} ions. With the use of relatively abundant elements associated to an attractive theoretical capacity of 147 mAh g^{-1} (65.7 $\mu Ah.cm^{-2}.\mu m^{-1}$ assuming a bulk density of 4.47 $g.cm^{-3}$) available at a high potential around 4.7 V, the LNMO material proves to be a very interesting thin film cathode material for Li-ion micro-batteries.

LNMO crystallizes in a spinel structure with Li^+ ions located on the tetrahedral sites and the transition metal ions on the octahedral sites in an oxygen cubic close packed network. The distribution of cations on the octahedral sites was found to depend on synthesis conditions.[4] Ni and Mn can either occupy the *4a* and *12d* sites of an ordered $P4_332$ space group or be randomly distributed in the *16d* sites of a disordered $Fd\bar{3}m$-type unit cell. [5] An order-to-disorder transition has been reported by several authors to occur above 700°C. [6-8] The transition is associated both with a loss of oxygen in the sample and the generation of Mn^{3+} ions in the spinel structure, which is identified by the onset of electrochemical activity of the material around 4.0 V vs Li/Li^+.

Some of us have recently reported the successful synthesis by magnetron sputtering of LNMO thin films and have shown that the deposition pressure allows controlling the Mn-Ni cation ordering. [9] Hence, disordered LNMO layers deposited at low pressure ($10^{-2} < P < 5.\ 10^{-2}$ mbar) and annealed at 700 °C were found to deliver the best electrochemical performance, i. e. an areal capacity of 50 $\mu Ah.cm^{-2}.\mu m^{-1}$ (77% of the theoretical value) and good capacity retention upon cycling. [9-11]

Many studies on the Li desintercalation/intercalation mechanism in bulk LNMO have highlighted its structure-dependency, with one-step or two-step phase transitions involving two or three cubic phases. [5-7,12-16] In the case of the ordered phase, two successive diphasic domains are identified during the electrochemical Li extraction/insertion reaction. [6,7,12] Differently, for the disordered one, a single-phase dominates the X-Ray Diffraction (XRD) pattern until the mid-charge ($x \sim 0.5$ in Li_xNMO) with a continuous shift in the position of the reflection lines indicating the existence of a solid solution. Then, a two-phase transition is observed during the second half of the charge. [7, 13-16] It is noteworthy that the degree of Ni/Mn disordering, which is strongly influenced by the synthesis and heat treatment conditions [5], was reported to extend the size of the solid-solution domain. [13] Moreover, as detailed by Hai et al. [17], independently of the order degree, the particle morphology (plate vs. octahedral crystals) has a strong impact on the size of the solid solution domain, and, as a consequence, on the spinel transport properties.

It is well known that nanosized electrode materials can exhibit different or improved performance compared to their bulk analogs. For instance, nanometric Li_xFePO_4 shows an increase of the two solid solution regions compared to the bulk material characterized by a wide two-phase Li insertion/extraction reaction and two narrow solid solution domains. [18,19] A similar phenomenon occurs for TiO_2 anatase, the particle size reduction leading to an increase of the Li_xTiO_2 solid solution region. [20] Furthermore, $Li_4Ti_5O_{12}$ nanoparticles were found to exhibit an increased storage capacity compared to the bulk powder ($Li_{8.5}Ti_5O_{12}$ versus $Li_7Ti_5O_{12}$, respectively) due to a higher surface/bulk ratio. [21-23] Considering LNMO, an enhanced rate capability has been reported for 500 nm size particles versus microsized powder [24] but the structural mechanism was not explored. Myung et al. [25] have performed an *ex situ* XRD study on LNMO nanocrystalline powders with particle size of about 50 nm in diameter and showed a reduced two-phase domain, beginning only by the end of charge, from the composition $Li_{0.2}$NMO. However, to our knowledge, investigation of the structural changes occurring in thin film LNMO electrode upon delithiation and lithiation has not been reported yet.

In this work, we report a detailed study of the Li insertion-extraction mechanism in sputtered LNMO thin films deposited on a multilayered Si/Al_20_3/Cr-Pt substrate during the first charge/discharge cycle. We show that controlled XRD and Raman *ex-situ* experiments provide relevant indication of phase transformation and changes in the Ni oxidation state in LNMO thin films during the first electrochemical cycle. Results of the XRD study reveal a solid solution region dominating the charging process, with the emergence of a second phase at 4.75 V. During the discharge, a reverse trend is observed, with a clear biphasic domain for ($0 < x \leq 0.3$ in Li_xNMO) followed by a wide solid solution region ($0.3 < x \leq 1$ in Li_xNMO). Remarkably, Raman spectra display significant variations on the high voltage plateau at ~ 4.7 V linked to the activity of the three $Ni^{2+}/Ni^{3+}/Ni^{4+}$ redox species. A thorough electrochemical and spectroscopic analysis gives access to a reliable determination of the LNMO thin film cathode state of charge (SOC) and discharge (SOD).

2. Results and Discussion

2.1. Thin film characterizations

Figure 1 presents the typical features of the radio frequency (RF) sputtered LNMO thin film. Figure 1a shows a schematic representation of the Si/Al_2O_3/Cr-Pt/LNMO stacking. Scanning Electron Microscopy (SEM) images (Figure 1b) allow measuring the LNMO film thickness to

be close to 400 nm. In addition, a good adhesion of the layers is found from the cross section analysis without any interdiffusion between the different layers. The top-view image gives a mean grain size of 200 nm diameter. The XRD pattern (Figure 1c) exhibits all the expected diffraction peaks of a pure LNMO phase (*Fd3̄m* space group, PDF: 01-080-2162). The refined cubic lattice parameter of 8.1437(10) Å is in good agreement with previous values reported for LNMO thin films, ranging from 8.167 to 8.105 Å, depending on the deposition pressure. [9] At this stage of the study, XRD patterns recorded with Cu based wavelength cannot distinguish the ordered from the disordered spinel structure because scattering factors at the Cu edge are too close to discriminate the $P4_332$ vs *Fd3̄m* space group. To overcome this problem, Raman spectroscopy was used to further investigate the thin films. Indeed, Raman spectroscopy is a relevant structural method to differentiate the ordered $P4_332$ and disordered *Fd3̄m* spinel structures thanks to its high sensitivity to the local symmetry. According to group theory, the number of expected Raman-active modes for the ordered spinel ($6A_1+14E+22F_2$) is much larger than for the disordered phase ($A_{1g}+E_g+3F_{2g}$). The Raman spectrum of the LNMO thin film (Figure 1d) exhibits 11 bands located at 164, 212, 340, 410, 491, 500, 513, 597, 615, 638 and 665 cm^{-1} typical of the *Fd3̄m* disordered structure. [7,16,26-29] Indeed, none of the additional bands characteristic of Ni and Mn species ordering in $P4_332$ space group can be detected (at 221, 240, 251, 293, 325, 378 and 462 cm^{-1}). [7,12,26,28,30] A full assignment of the LNMO Raman fingerprint has been previously provided by analogy with the parent compound LMO. [16, 26-32] A common feature of high voltage spinel Raman spectra is the strong A_{1g} band between 450 and 700 cm^{-1} and a group of bands between 100 and 450 cm^{-1} of weaker intensity. Previous experimental [16,26-30] and theoretical [31,32] studies have shown that the intense A_{1g} peak at 638 cm^{-1} corresponds to the stretching of the *16d* site cations M–O bonds in the MO_6 octahedra (M = Mn, Ni). The splitting of this mode is ascribed to vibrations of Mn^{4+}–O bonds (at 597 cm^{-1}), Ni-O bonds at 615 cm^{-1} and a mixture of Mn–O and Ni–O bonds at 638 cm^{-1}. The weak shoulder at 665 cm^{-1} has F_{2g} symmetry and originates from bending vibrations of the *16d* cations M–O bonds. Another rather intense Raman active mode of F_{2g} symmetry is observed at 500 cm^{-1} with two weak additional components at 491 and 513 cm^{-1}. This $F_{2g}(2)$ mode is reported as a pure Ni-O stretching mode, [16,28,29,32] which suggests that its position and intensity should be impacted by a change in the oxidation state of Ni. The phonon lines at 340 and 410 cm^{-1} correspond to the E_g symmetrical M–O–M deformation modes. [28,32] Finally, the lowest energy $F_{2g}(1)$ phonons at 164 and 212 cm^{-1} are predominantly due to lattice translation modes. [33]

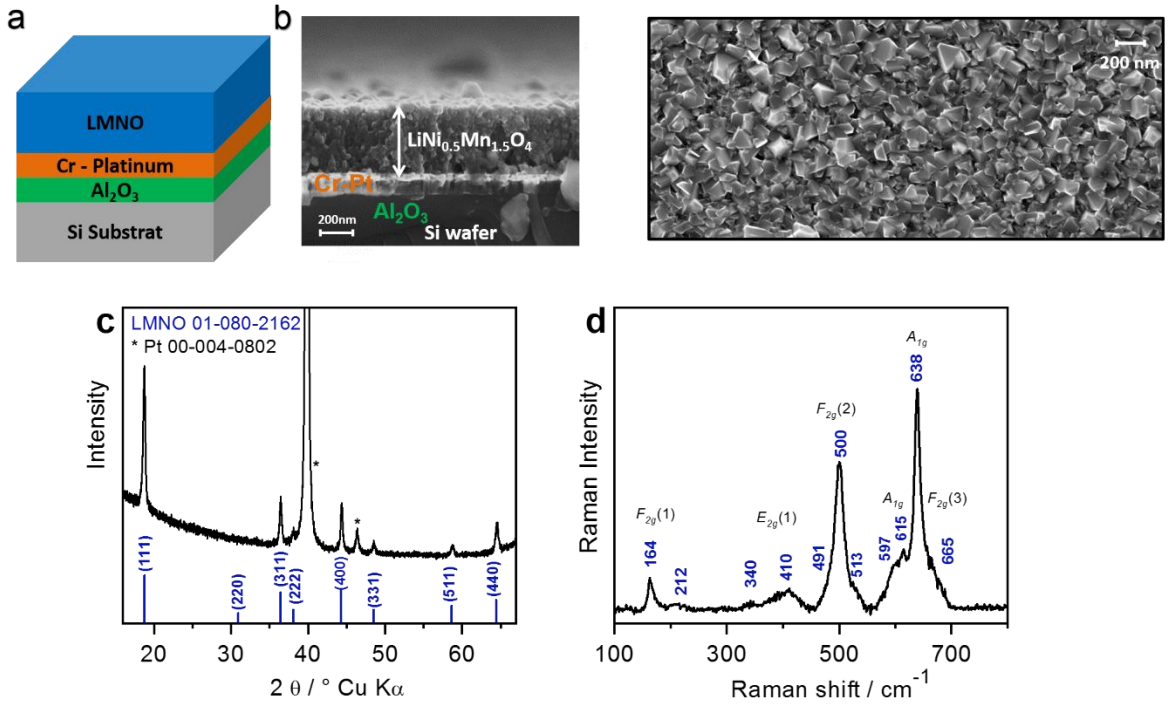

Figure 1. (a) Schematic view of the Si / Al_2O_3 / Cr / Pt / LNMO layer stacking. (b) SEM images showing the top and cross sections views of the Si / Al_2O_3 / Cr / Pt / LNMO staking. (c) XRD pattern of the LNMO thin film. (d) Raman spectrum of the LNMO thin film with band assignment indicated in italic character.

2.2. Electrochemical properties

The electrochemical features of the LNMO thin film are reported in **Figure 2**. Cyclic voltamperometry experiments between 4.4 and 4.8 V vs. Li^+/Li performed at a scan rate of 0.1 $mV \cdot s^{-1}$ (see insert in Figure 2a) evidence two oxidation peaks at 4.69 and 4.76 V corresponding to the successive oxidation of the nickel element (Ni^{2+} to Ni^{3+} and Ni^{3+} to Ni^{4+}). This process is reversible, as demonstrated by the presence of two corresponding peaks during the reduction process, located at close potentials of 4.65 and 4.70 V, respectively.
The initial charge capacity of the LNMO thin films (**Figure S1**) is about 400 µAh cm^{-2} .μm^{-1} for a reversible capacity of about 55 µAh cm^{-2} .μm^{-1}. This huge irreversible first charge capacity is commonly observed for LNMO, especially when developing large surface area such as in the present case of thin films. [34] This phenomenon is related to electrolyte decomposition, probably enhanced in the present flat cell configuration exposing the thin film electrode to a large amount of electrolyte. This is further evidenced during the second cycle (see blue dashed line in Figure 2a) where the charge capacity remains as high as 118 µAh cm^{-2}.μm^{-1} while the discharge curve completely superimposes the first one. The detection of a

small redox activity at ~ 4.1 V during the first charge (see Figure S1) is due to the Mn^{3+}/Mn^{4+} redox couple and deserves also a comment. This redox activity is commonly attributed to oxygen deficiency in the films owing to the high temperature of the post deposition annealing. [9] Indeed, to compensate the oxygen deficiency, a few Mn^{4+} ions are reduced to Mn^{3+}. Similar results have been previously reported for bulk and thin films LNMO electrodes. [5,35,36]

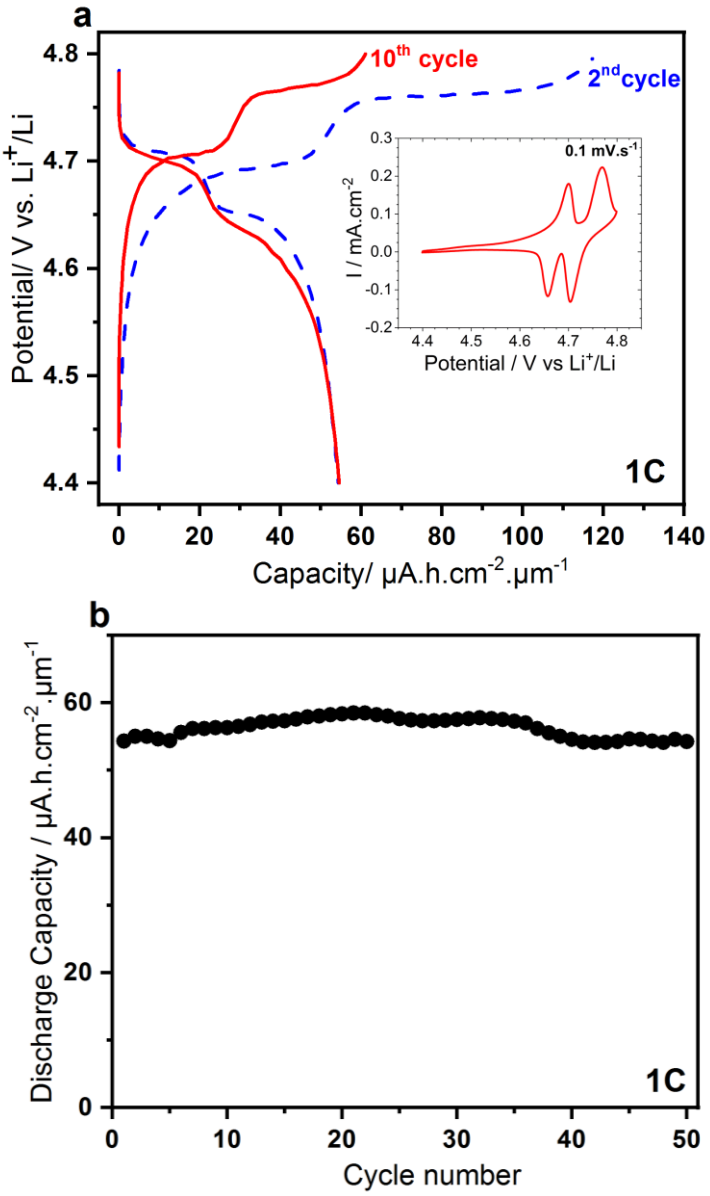

Figure 2. Electrochemical performance of the LNMO thin film in the 4.4 –4.8 V vs Li/Li^+ voltage window. (a) Typical charge-discharge curve at 1C rate (10^{th} cycle); (b) Evolution of the discharge capacity vs the number of cycles number at 1C rate. In insert: CV profile at 0.1 $mV.s^{-1}$.

The typical charge-discharge curve of the present LNMO thin film (displayed for the 10^{th} cycle, see red straight line in Figure 2a) exhibits a large plateau with two well-marked steps at

4.70 and 4.77 V characteristics of disordered LNMO.[17,35-39] Indeed, as theoretically demonstrated using DFT calculations, the Ni^{2+}/Ni^{3+} and Ni^{3+}/Ni^{4+} redox potentials and their gap are related to the ordering cation level.[40] The disordered Li_xMNO phase would be compatible with stable Li and vacancy (Vac) rearrangements (Li/Vac ordering) for $0.5 \leq x \leq 1$, leading to a lower working potential in this composition region. The most stable form corresponds to Li and Vac organized in a zigzag form for x = 0.5.[40] For the ordered LMNO phase, there is no favorable Li/Vac rearrangement and therefore not significant potential jump for x = 0.5.[17,37,39]

A discharge capacity value of 55 $\mu Ah.cm^{-2}.\mu m^{-1}$ can be reached here at 1C rate, which matches perfectly the theoretical one considering the 20% porosity of the sputtered LNMO thin films.[9, 41] A good capacity retention is attained over at least 50 cycles (Figure 2b), which indicates the good adhesion of the thin films and suggests moderate structural changes during the electrochemical reaction. The LNMO/Li half-cell exhibits similar or little higher electrochemical performance than that reported for 200 nm sol-gel prepared LNMO thin films post annealed at 700°C (~ 44 $\mu Ah.cm^{-2}.\mu m^{-1}$ stable over 100 cycles)[42] and 400 nm RF sputtered LNMO thin films annealed in air at 700°C for 1h (~ 40 $\mu Ah.cm^{-2}.\mu m^{-1}$).[34] Accordingly, the structural changes of the LNMO thin film cathode material during the charge/discharge were investigated using XRD and Raman spectroscopy.

2.3. Study of the structural changes during the first charge-discharge cycle

2.3.1. XRD study

From the starting open circuit voltage (OCV) potential of ~ 3.3 V, several LNMO thin film electrodes have been oxidized at constant current (I = 8 µA) up to different cutoff voltages during the course of the first charge (e.g. 4.4, 4.65, 4.725, 4.75 and 4.8 V, see filled circles in **Figure 3a**). The full XRD patterns collected for these charged electrodes are gathered in Figure 3b. Enlarged views showing the (*111*), (*400*) and (*440*) LNMO reflections evolutions are shown in Figure 3c. These XRD data indicate that the cubic structure of the pristine LNMO thin film is retained upon oxidation. Between 4.4 and 4.725 V, i.e. during the first half of the potential plateau, a continuous shift of LNMO reflections toward higher angles is observed (see Figure 3c), pointing to a shrinkage of the unit cell parameter through a solid solution behavior.

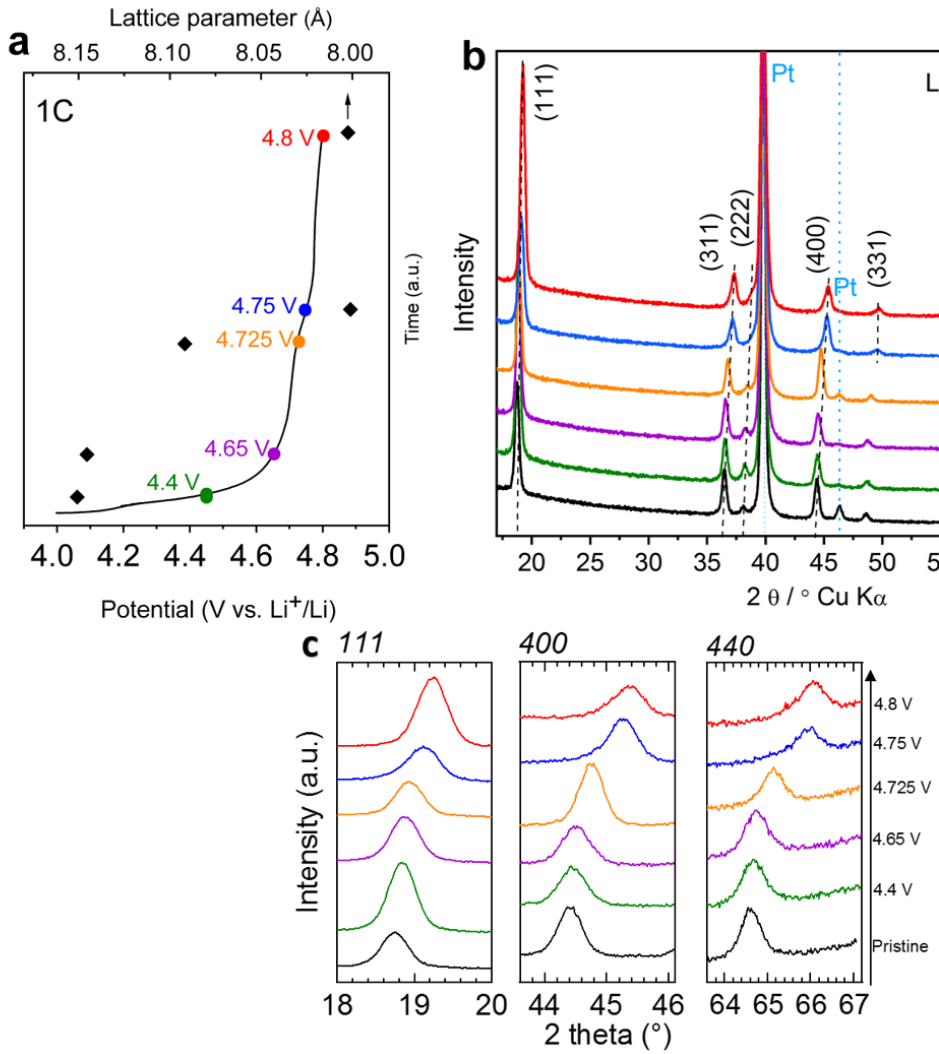

Figure 3. *Ex situ* XRD study of the LNMO thin film during the first charge from OCV to 4.8 V vs Li/Li$^+$. (a) Charge curve performed at 8 µA.cm^{-2} showing the cutoff voltage of the investigated electrodes (filled circles) and refined cubic lattice parameter for each investigated electrode (black diamonds); (b) XRD patterns recorded for the different charged electrodes. In black: XRD pattern of the pristine electrode, (c) Enlarged view of the XRD patterns showing the *111*, *400* and *440* reflections of LNMO. Color code in Figs 3b-c refers to the SOCs designated by colored symbols in Fig.3a.

Indeed, the cubic lattice parameter issued from pattern matching Lebail refinement (**Table S1**) is found to decrease from 8.1437(10) Å for the pristine material to 8.0918(6) Å for the electrode charged at 4.725 V (see black diamonds in Figure 3a), i. e. close to the cell parameter value of $Li_{0.5}NMO$ reported in the literature. [43] At 4.75 V, a sudden shift of the LNMO peaks is observed which corresponds to a cell parameter decreasing to 8.0025(9) Å, close to that reported for NMO.[43] These observations indicate the appearance of a second

cubic phase from the mid-discharge, namely the fully delithiated NMO phase. Note however that the existence of a biphasic domain where NMO and the intermediate $Li_{0.5}$NMO phase would coexist cannot be completely discarded at the stage of the present analysis, especially because of insufficient intrinsic resolution of the micro-diffraction optics and/or small crystallite size, leading to broad XRD peaks.

From the end of charge at ~ 4.8 V corresponding to the NMO composition, several thin film electrodes have been reduced at constant current (I = 4 µA) in the 4.8 –4.4 V vs Li/Li^+ voltage range to reach different x values in Li_xNMO ($0 \leq x \leq 1$) indicated by filled circles in **Figure 4a**. The collection of XRD patterns recorded during the discharge is shown in Figure 4b. Enlarged views showing the (*111*), (*400*) and (*440*) LNMO reflections evolutions are displayed in Figure 4c. At the beginning of the discharge, from x = 0.1, one observes the appearance of a second diffraction peak, all the more visible at highest angles, i. e. for the (*400*) and (*440*) reflections. Indeed, in the $0.1 \leq x \leq 0.3$ region, the consideration of one single phase does not allow a correct match of the calculated XRD patterns to the experimental ones, even with the poor resolution already pointed out. Hence, refinements of the cell parameters were carried out by considering two cubic structures with slightly different lattice parameters. The results of these refinements are presented in Figure 4d and Table S1. It is then clear that in the $0.1 \leq x \leq 0.3$ composition range, two phases coexist, namely NMO and Li_xNMO ($x \approx 0.3$), with cell parameters of 7.9992(10) Å and 8.0649(12) Å, respectively. The NMO cell parameter remains practically unchanged when the second phase emerges, then both unit cell parameters decrease for x = 0.2, to 7.9961(9) Å and 8.0583(17) Å, respectively. For x = 0.3, the lattice parameters of the two phases increase by ~ 0.2 %. From x = 0.4, the NMO phase disappears and a single-phase domain of Li_xNMO is observed up to the end of the discharge (x = 1). In this $0.4 \leq x \leq 1$ composition range, a linear shift of the Li_xNMO peaks is clearly observed (Figure 4c), characteristics of a solid solution reaction where the unit cell parameter increases from 8.0864(7) Å to 8.1567(13) Å (Figure 4d). The diffraction pattern of the thin film electrode discharged to 4.4 V matches that of the pristine one (Figures 4b-4c), showing that the LNMO structure is not altered after the first charge / discharge cycle.

The present XRD study of the sputtered LNMO thin film evidences an overall unit cell decrease upon the first charge, and a reverse trend upon discharge. This unit cell shrinkage-dilation breathing of less than 2 % is very comparable to that reported for bulk LNMO electrodes. [5-7, 12-16, 25] and is one of the reasons of the good cyclability of the LNMO thin films (Figure 2b). The structural changes experienced by the LNMO thin film involve a solid solution upon Li extraction up to the mid-charge, followed by the emergence of a new cubic

phase during the second part of the charge. Slightly differently, the discharge process is found to involve a short ill-defined biphasic region below 0.3 Li followed by a solid solution over a wide $0.4 \leq x \leq 1$ composition range. This structural evolution during the discharge exhibits strong similarities with that reported for bulk *Fd3̄m* LNMO. [7,13-16]

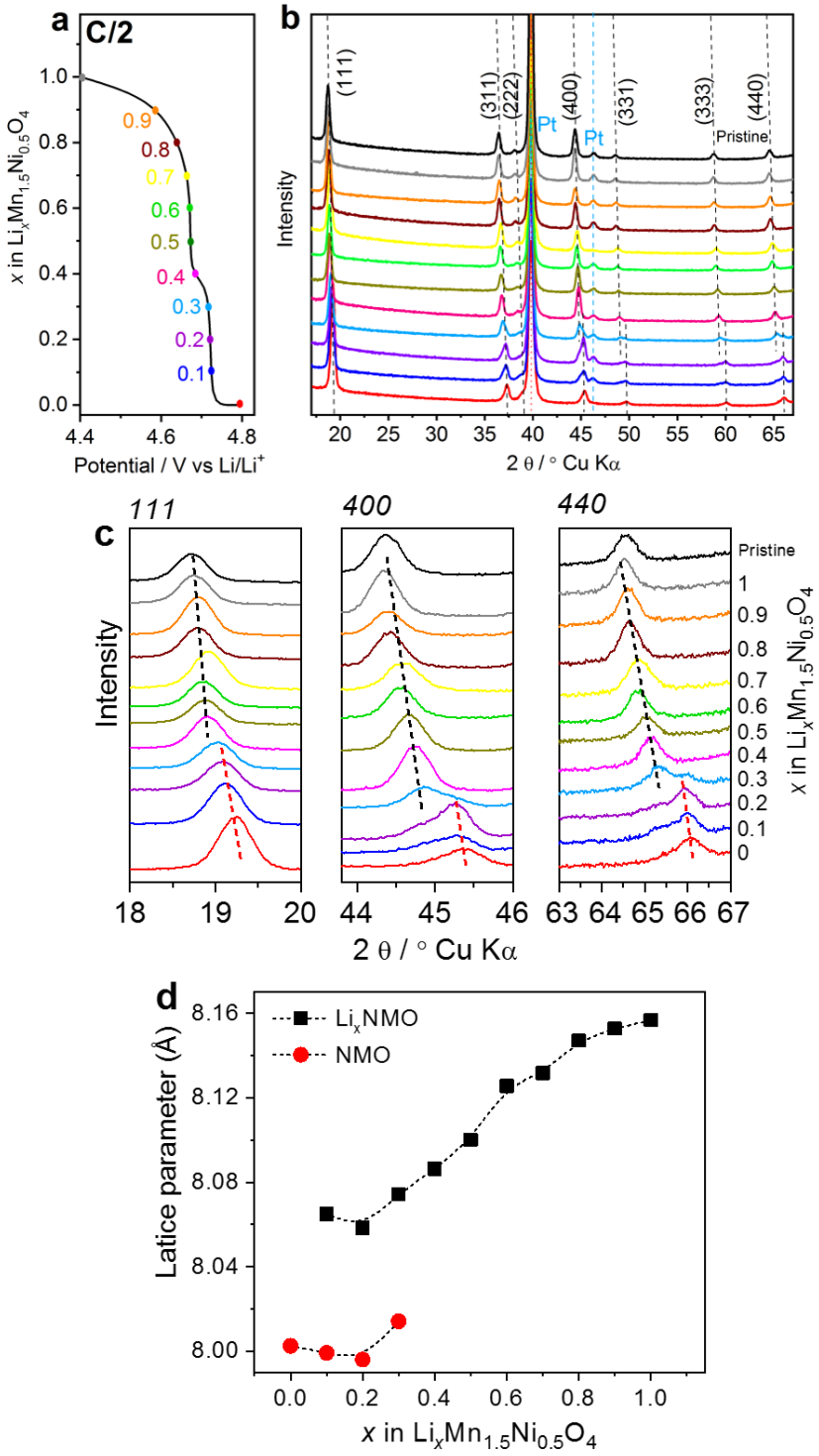

Figure 4. *Ex situ* XRD study of the LNMO thin film during the first discharge from 4.8 to 4.4 V vs Li/Li$^+$. (a) Discharge curve at C/2 rate (4 µA.cm^{-2}) showing the lithium content (x) in

$Li_xNi_{0.5}Mn_{1.5}O_4$ electrodes. (b) XRD patterns recorded for the discharged electrodes. In black: XRD pattern of the pristine thin film electrode. (c) Enlarged view of the XRD patterns showing the *111*, *400* and *440* LNMO reflections; (d) Refined cubic lattice parameters of the different phases as a function of the lithium content (x) in $Li_xNi_{0.5}Mn_{1.5}O_4$. Color code in Figs 4b-c refers to the DODs designated by colored filled circles in Fig.4a.

2.3.2. Raman spectroscopy study

The Raman spectra of the LNMO thin film electrodes recorded during the first charge-discharge are gathered in **Figure 5**. Note that whatever the SOC or DOD, similar spectra were found for the 10 investigated points on each sample, which indicates the good homogeneity of the electrochemical reaction in the LNMO thin film. A careful examination of the Raman spectra collection during the charge from OCV (3.3 V) to 4.8 V (Figure 5a) leads to the following comments:

(i) The fingerprint of the pristine LNMO electrode, with Raman bands at 164, 212, 340, 410, 491, 500, 514, 597, 615, 638 and 665 cm^{-1}, is kept for the electrode charged at 4.4 V. This indicates that the few Mn^{3+} ions that oxidize into Mn^{4+} in this potential range do not induce noticeable change in the Mn–O bond lengths. Indeed, similar sized MnO_6 octahedra are observed in the structure upon LNMO delithiation. [43]

(ii) From E = 4.65 V, the spectral profile undergoes progressive changes, especially in the 450-700 cm^{-1} region corresponding to the $F_{2g}(2)$ and A_{1g} modes (Figure 1d). As written above, the $F_{2g}(2)$ symmetry specie at 500 cm^{-1} involving pure Ni–O stretching vibrations is a relevant descriptor of the Ni–O bond. Indeed, looking carefully Figure 5a, this mode is strongly affected as soon as the Ni redox system is involved: At E = 4.65 V, a new component appears at 535 cm^{-1} to be the major band in the $F_{2g}(2)$ region at the mid-charge voltage of 4.725 V while the band at 500 cm^{-1} has practically vanished. At the same potential of 4.725 V, a new component is detected at 542 cm^{-1} that increases at the expense of the 535 cm^{-1} one during the second half of the charge (E > 4.725 V). At the end of the charge (E = 4.8 V), the Raman spectrum exhibits one single high intensity peak at 542 cm^{-1}.

(iii) From E = 4.725 V, i.e. when all the Ni^{2+} ions have been oxidized into Ni^{3+}, a strong intensity decrease is observed for the strong A_{1g} mode at 638 cm^{-1} involving both Mn–O and Ni–O stretching vibrations.

Reverse spectral changes are displayed during the discharge (Figure 5b) and the complete restoration of the Raman spectrum of the LNMO thin film is seen at 4.4 V, with the whole

bands at 164, 212, 340, 410, 491, 500, 514, 597, 615, 638 and 665 cm^{-1}. This result demonstrates the excellent reversibility of the lithium extraction-insertion process at the scale of the chemical bond.

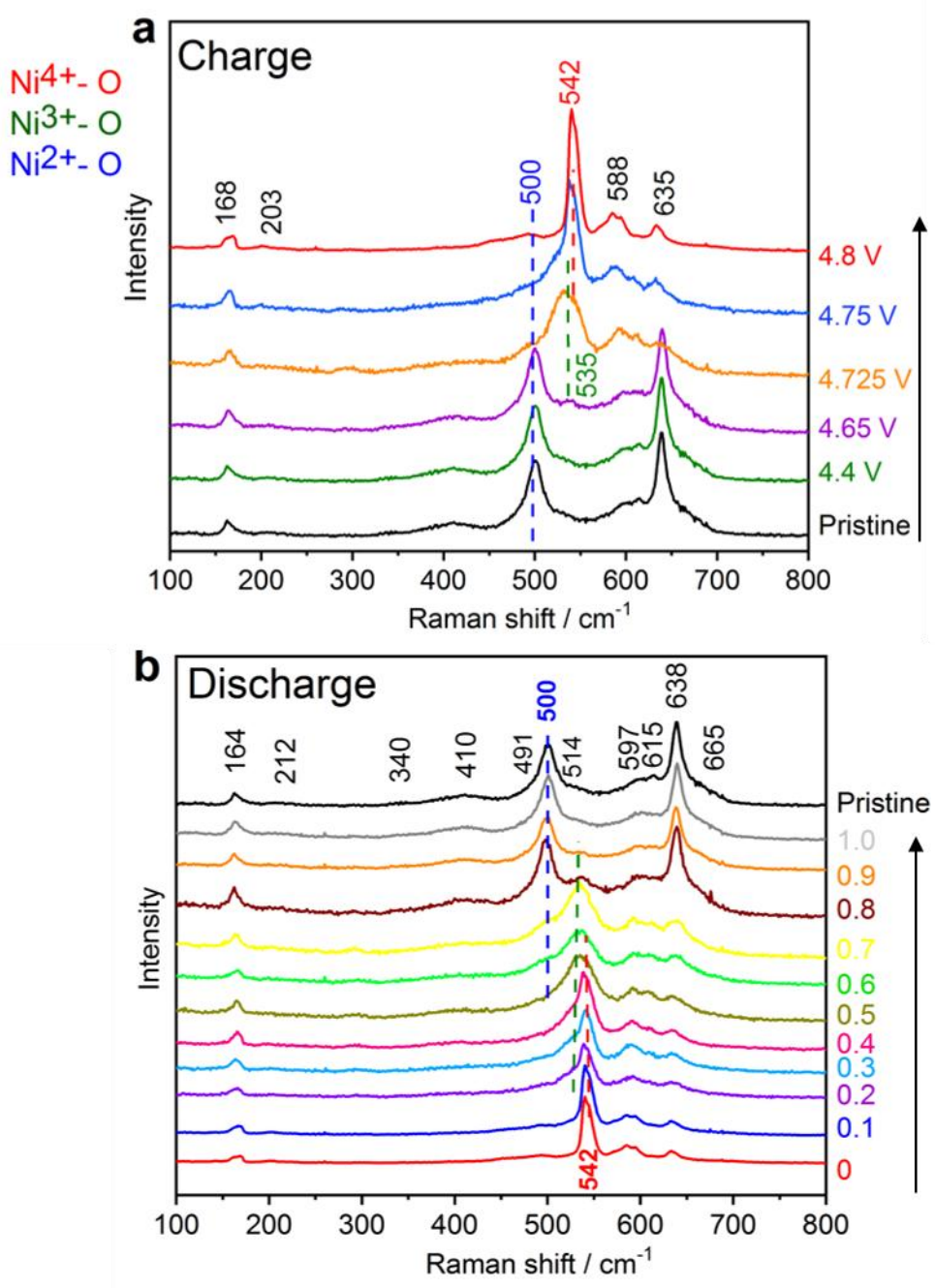

Figure 5. *Ex situ* Raman spectra of the LNMO thin films during (a) the first charge from OCV to 4.8 V vs Li/Li^+ and (b) the first discharge from 4.8 to 4.4 V Li/Li^+, as a function of the lithium content (x) in $Li_xNi_{0.5}Mn_{1.5}O_4$ electrodes. Color code in Figs 5a and 5b refers to the SOC and DOD designated by colored filled circles in Figs.3a and 4a, respectively.

These Raman data indicate that the spectral changes in the $F_{2g}(2)$ region are precisely related to the Ni redox state variations, increasing successively from +2 to +3 and +4 upon charge

and the reverse trend during the discharge. As recently reported for bulk electrodes, [16] the 500, 530-535 and 542 cm^{-1} Raman bands are assigned to the Ni^{2+}–O, Ni^{3+}–O and Ni^{4+}–O stretching vibrations, respectively. The higher wavenumber of the $F_{2g}(2)$ mode with the increasing Ni redox state reflects a strengthening/shortening of the Ni–O bond upon Li extraction. This result is consistent with the smaller sized NiO_6 octahedra found upon LNMO delithiation, with Ni–O bond length values of 2.07 and 1.88 Å for LNMO and NMO, respectively. [43,44] Furthermore, in the higher wavenumber region where mixed Mn and Ni vibration occur, the relative intensity variation of the strongest component at 638 cm^{-1} suggests a major participation of Ni^{2+}–O vibration to this mode.

Further quantitative information is accessible through the analysis of the Raman relative intensities in the 450-700 cm^{-1} wavenumber range. Indeed, the Raman spectrum profile in the $F_{2g}(2)$ region is directly linked to the proportion of Ni^{2+}, Ni^{3+} and Ni^{4+} species in the cathode, which can be estimated from the relative areas of the $F_{2g}(Ni^{2+})$, $F_{2g}(Ni^{3+})$ and $F_{2g}(Ni^{4+})$ components at 500, 530-535 and 542 cm^{-1}, respectively. Raman spectra fittings during the charge and the discharge (selected results are displayed in **Figure S2** and **Figure 6**, respectively) allow estimating the fraction of the different Ni redox species, which is directly linked to the Li content in the thin film. The overall results are gathered in **Table 1**. It is then clear that during the first charge, $Ni^{2+} \rightarrow Ni^{3+}$ oxidation starts between 4.4 V and 4.725 V, with 14% and 87 % produced Ni^{3+} species at voltage of 4.65 and 4.725 V, respectively. At 4.75 V, all the Ni^{2+} ions have been oxidized into Ni^{3+} and Ni^{4+} species and the estimated Li content in the thin film is x = 0.225. At 4.8 V, only Ni^{4+} species are detected, which demonstrates the full Li extraction from the electrode (x = 0).

It is noteworthy to comment the evolution of the relative amounts of the different Ni redox species during the discharge, displayed in Figure 6 and **Figure 7**. From the fully charged sample (x = 0), the $Ni^{4+} \rightarrow Ni^{3+}$ reduction immediately takes place, illustrated by a decrease of the relative amount of Ni^{4+} (see red dashed line in Figure 7) at the benefit of Ni^{3+} (green dashed line) in the $0 < x \leq 0.5$ composition range. Then, a quasi-quantitative $Ni^{3+} \rightarrow Ni^{2+}$ transformation occurs for x > 0.5, manifesting itself through an abrupt decrease of Ni^{3+} ions content at the benefit of Ni^{2+} species. The evolution of the Ni^{2+}, Ni^{3+} and Ni^{4+} relative amounts as a function of x in Li_xNMO electrodes calculated from Raman spectra fittings (represented by colored symbols in Figure 7) are very close to those expected from the faradaic yield involved during the electrochemical preparation (see solid line in Figure 7). This result demonstrates the reliability of the present Raman analysis and its efficiency to provide a good estimation of the thin film cathode composition.

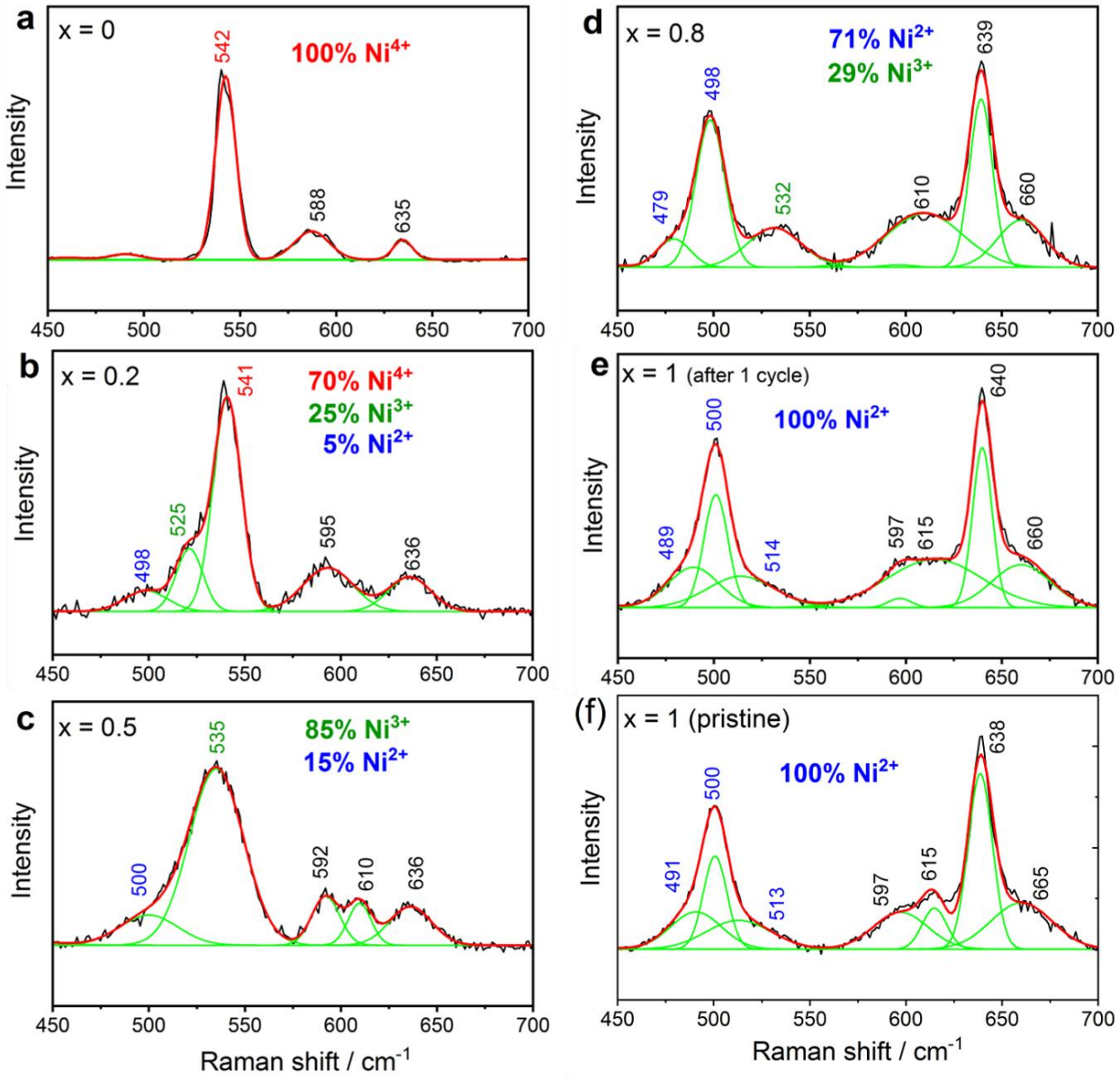

Figure 6. (a-e) Selection of Raman spectra fittings during the first discharge of Li_xNMO thin films ($0 \leq x \leq 1$). (f) Raman spectrum of the pristine LiNMO thin film.

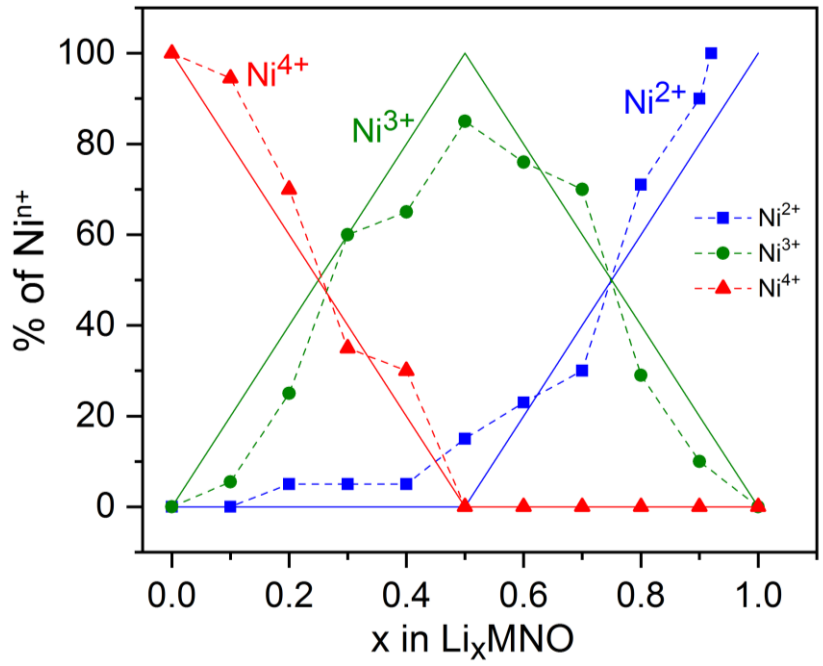

Figure 7. Evolution of the $Ni^{2+}/Ni^{3+}/Ni^{4+}$ ratio during the first discharge of the LiNMO thin film samples. Symbols connected by dashed lines: values obtained from the quantitative analysis of the Raman spectra. Solid lines: expected values derived from the faradaic yield involved during the electrochemical samples preparation.

	Cutoff voltage (V)	Ni^{2+} (%)	Ni^{3+} (%)	Ni^{4+} (%)	Estimated x in Li_xNMO
CHARGE	3.3 (OCV)	100	0	0	1
	4.4	100	0	0	1
	4.65	94	6	0	0.97
	4.725	13	87	0	0.565
	4.75	0	45	55	0.225
	4.8	0	0	100	0

	x in Li_xNMO	Ni^{2+} (%)	Ni^{3+} (%)	Ni^{4+} (%)
DISCHARGE	0	0	0	100
	0.1	0	5	95
	0.2	5	25	70
	0.3	5	60	35
	0.4	5	65	30
	0.5	15	85	0
	0.6	23	76	0
	0.7	30	70	0
	0.8	71	29	0
	0.9	90	10	0
	1	100	0	0

Table 1. Relative abundance of Ni^{2+}, Ni^{3+} and Ni^{4+} species in the $Li_{1-x}MNO$ electrodes during the first charge-discharge cycle calculated from Raman spectra fittings shown in Figures 6 and Figure S2.

3. Conclusion

This study reports the investigation of the structural changes in a disordered sputtered LMNO thin film cathode deposited on a functional Si/Pt current collector during lithium deintercalation/ intercalation in the 4.4 V – 4.9 V voltage range. Complementary XRD and Raman experiments lead to a detailed picture of phase transformation and changes in the Ni oxidation state in the LNMO thin films during the first electrochemical cycle. The phase transition mechanism during the discharge consists in a narrow diphasic region followed by a wide solution domain, with the occurrence of two cubic phases, similar to that reported for bulk disordered LNMO. An overall unit cell decrease is observed upon the first charge, and a reverse trend upon discharge, with a unit cell shrinkage-dilation breathing of less than 2 % close to that reported for bulk LNMO electrodes. On the other hand, the great sensitivity of Raman spectroscopy to nanostructures has allowed gaining significant information on the atomic-scale induced structural changes in the LNMO thin films. Actually, important spectral variations are observed on the high voltage plateau at ~ 4.7 V corresponding to changes in the Ni redox state. Appropriate analysis of the Raman spectra reveal the existence of the three Ni^{2+}, Ni^{3+} and Ni^{4+} redox species and give access to their relative amounts in the charged and discharged thin film electrodes. The 2-phase Li extraction insertion mechanism here provided for the first time for the LNMO cathode in thin film configuration is consistent with the disordered nature of the layers and explain their good electrochemical performance.

4. Experimental Section

Thin film synthesis: A 50 nm thick Al_2O_3 insulating layer, acting as a diffusion barrier, [9-11] was deposited on a (*100)*-oriented silicon wafer (diameter = 3 inch) by Atomic Layer Deposition (ALD) from a PicoSun R200 reactor. Then, a metallic current collector based on Chromium (3 nm-thick) and Platinum (50 nm-thick) layers was evaporated on the oxide layer using a Plassys MEB 550S instrument. The Cr layer favors a better adhesion of the LNMO thin film on the Pt current collector, enabling to produce thick LNMO layers without mechanical issues such as delamination. [10] LNMO thin films 400 nm thick were deposited on this Si/ Al_2O_3/ Cr-Pt substrate by radio frequency magnetron sputtering in a CT-200 cluster from Alliance Concept using a pure LNMO target from TOSHIMA Japan (99.999 %, 10 cm diameter. 6 mm thick) under an argon atmosphere at room temperature. [9-11] The deposition

was achieved at 600 °C and 2.5 10^{-2} mbar. Then, an annealing is carried out at 700 °C for 2 h under air in order to crystallize the LNMO thin films. [7]

Characterizations: The morphology (top view and cross-section) as well as the thickness of the thin layers were analyzed using a Zeiss supra 55-VP scanning electron microscope. The structural XRD studies were conducted with a Rigaku Smartlab diffractometer equipped with a copper rotating anode type generator delivering 9kW power (lambda = 1.5418 Å) and a Rigaku DTEX-Ultra 250 silicon-strip 1D detector allowing simultaneous 3° data acquisition. One of the main advantages of this diffractometer is its versatility. Indeed, two different configurations were used in the present work: i) a Bragg-Brentano reflection mode misaligned by 2 ° to avoid the detector saturation by the extremely high intensity of the (*400*) peak of the monocrystalline silicon substrate, 2θ = 69.13 °. This configuration was used during the optimizations process of the layers as well as to identify the obtained phases; ii) a reflection - parallel beam (multilayer mirror) and focusing optics (Rigaku CBO-f polycapillary type) allowing to condense all the intensity on a 400 µm spot, and thus to precisely localize one zone or another. This configuration was used to study the thin film evolution during electrochemical charge-discharge.

Raman spectra were recorded with a LaBRAM HR 800 (Jobin-Yvon- Horiba) Raman micro-spectrometer including Edge filters and equipped for signal detection with a back illuminated charge coupled device detector (Spex CCD) cooled by Peltier effect to 200 K. A He:Ne laser (632.8 nm) was used as the excitation source. The spectra were measured in back-scattering geometry. The spectral resolution was about 0.5 cm^{-1}. A 100× objective was used to focus the laser light on sample surface to a spot size of 1 μm^2. The power of the laser beam was adjusted to 0.2-0.5 mW with neutral filters of various optical densities in order to prevent laser-induced damage of the sample. Raman spectra were systematically recorded on 10 different spots of each sample, which give similar fingerprints, showing the homogeneity of the electrochemical reactions in the thin films.

Electrochemical tests: Electrochemical measurements were carried out in homemade Teflon flat cells operated in an Ar filled glove box. The cell was composed of two pieces of Teflon where the samples are sandwiched between the pieces. A hole of 0.442 cm^2 was drilled in the top piece, allowing filling the flat cell with the liquid electrolyte (2 mL of 1 M $LiClO_4$ dissolved in ethyl carbonate (EC)/ dimethylcarbonate (DMC) (1:1). An O-ring was used to seal the sample / top piece interface and to define an analyzed electrode surface area of 0.442 cm^2. The cells were assembled with LNMO thin film as working electrode (0.6 mg) and pure

Li as both counter and reference electrode. Galvanostatic cycling and cyclic voltamperometry (CV) were performed with a multichannel Biologic VMP3 potentiostat.

The structural investigation was carried out in the 4.4 – 4.8 V vs Li/Li^+ potential window by using the electrochemical flat cell, during the first charge-discharge cycle of the LNMO thin film. The cell was charged at C rate (8 µA, 18–20 µA. cm^{-2}) and discharged at C/2 rate (4 µA, 9–10 µA. cm^{-2}) up to the required states of charge (SOCs) and depths of discharge (DODs). The cell was then disassembled in the glove box. The thin film was rinsed 3 times with DMC in order to remove any electrolyte residues and placed in appropriate airtight sample holders to be further analyzed by XRD and Raman spectroscopy. XRD experiments were carried out using a microdiffraction configuration on each electrode area (~ 7 mm diameter). A programmable X-Y table allowing translations was used to check the homogeneity of the analysis. We realized a mapping of these zones decomposed into 8 distinct analyses in steps of 1 mm. On each analysis of 400 µm in lateral size (the longitudinal size depends on the incidence angle), all the power of the rotating anode was focused on the spot to achieve a remarkable beam brilliance for a laboratory machine, and allowing relatively fast acquisitions. The acquisition time was set to 15 min for Bragg angles between 15 and 70° with a step of 0.01°. Note that in order to increase the statistics and the signal-to-noise ratio of the reported patterns, once we verified that the 8 measurements were indeed identical, and thus the homogeneity of the analysis zone, we summed the 8 measurements, which finally corresponded to measurement time of 2h per zone. Cell parameters were refined, as well as profile ones (i.e. peak shapes using a pseudo-Voigt model, background parameters, asymmetry parameters and zero-point correction) by full pattern matching of the summed diffractogram using the JANA2006 software. [45] Estimated standard uncertainty were multiplied by Berar's factor to give more realistic values. All numerical values are given in supplementary materials, **Table S1.**

Supporting Information

Supporting Information is available from the Wiley Online Library or from the author.

Acknowledgements

The authors thank the French ANR within the CASSIOPES project (ANR-17-CE09-0016-01) for financial support. The French network on electrochemical energy storage (RS2E) and the Store-Ex Labex are also thanked for their support. The French RENATECH network is greatly acknowledged for the use of microfabrication facilities. Chevreul Institute (FR 2638),

Ministère de l'Enseignement Supérieur et de la Recherche, Région Hauts de France and FEDER are acknowledged for supporting and funding XRD facilities.

ClL, MH and ChL were involved in the films deposition of the materials and the electrochemical analyses. ClL and PR performed the X-Ray diffraction analysis of the LNMO films. Raman and electrochemical analyses were achieved by AB, JPPR and RBH. RBH, JPPR & AB planned the project and wrote the paper. All the authors discuss about the obtained results and approve the manuscript before submission.

Received: ((will be filled in by the editorial staff))
Revised: ((will be filled in by the editorial staff))
Published online: ((will be filled in by the editorial staff))

References

[1] J. P. Pereira-Ramos, R. Baddour-Hadjean, in *Lithium Ion Rechargeable Batteries* **2009**, 257-311. Ed. K. Ozawa, Wiley-VCH Verlag GmbH.

[2] A. Patil, V. Patil, D. W. Shin, J-W. Choi, D-S. Paik, S-J. Yoon, *Mater. Res. Bull*. **2008**, *43*, 1913.

[3] T. Ohzuku, S. Takeda, M. Iwanaga, *J. Power Sources* **1999**, *81-82*, 90.

[4] J. Yang, X. Han, X. Zhang, F. Cheng, J. Chen. *Nano Res.* **2013**, *6*, 679.

[5] A. Manthiram, K. Chemelewski, E.-S. Lee, *Energy Environ. Sci.* **2014**, *7*, 1339.

[6] J.-H. Kim, S.-T. Myung, C. S. Yoon, S. G. Kang, Y.-K. Sun, *Chem. Mater.* **2004**, *16*, 906.

[7] M. Kunduraci, G. G. Amatucci, *J. Electrochem. Soc.* **2006**, *153* (7), A1345.

[8] M. Kunduraci, G. G. Amatucci, J. *Power Sources* **2007**, 165, 359.

[9] M. Létiche, M. Hallot, M. Huvé, T. Brousse, P. Roussel, C. Lethien, *Chem. Mater.* **2017**, *29* (14), 6044.

[10] M. Hallot, A. Demortière, P. Roussel, C. Lethien, *Energy Storage Mater.* **2018**, *15*, 396.

[11] M. Hallot, B. Caja-Munoz, C. Leviel, O. I. Lebedev, R. Retoux, J. Avila, P. Roussel, M. C. Asensio, C. Lethien, *ACS Appl. Mater. Interfaces* **2021**, 13, 15761.

[12] K. Ariyoshi, Y. Iwakoshi, N. Nakayama, T. Ohzuku, *J. Electrochem. Soc.* **2004**, *151* (2), A296.

[13] H. Duncan, B. Hai, M. Leskes, C. P. Grey, G. Chen, *Chem. Mater*. **2014**, *26*, 5374.

[14] R. Alcántara, M. Jaraba, P. Lavela, J. L. Tirado, *Electrochim. Acta* **2002***, 47*, 1829.

[15] J. Zheng, J. Xiao, X. Yu, L. Kovarik, M. Gu, F. Omenya, X. Chen, X.Q. Yang, J. Liu, G. L. Graff, M. S. Whittingham, J. G. Zhang, *Phys. Chem. Chem. Phys*. **2012**, *14*, 13515.

[16] A. Bhatia, Y. Dridi Zrelli, J. P. Pereira-Ramos, R. Baddour-Hadjean, *J. Mater. Chem. A* **2021**, *9*, 13496.

[17] B. Hai, A. K. Shukla, H. Duncan, G. Chen, *J. Mater. Chem. A* **2012**, *1* (3), 759.

[18] N. Meethong, H.-Y. S. Huang, W. C. Carter, Y.-M. Chiang, *Electrochem. Solid State Lett.* **2007**, *10* (5), A134.

[19] G. Kobayashi, S. Nishimura, M.-S. Park, R. Kanno, M. Yashima, T. Ida, A. Yamada, *Adv. Funct. Mater.* **2009**, *19* (3), 395.

[20] M. Wagemaker, W. J. H. Borghols, F. M. Mulder, *J. Am. Chem. Soc.* **2007**, *129* (14), 4323.

[21] W. J. H. Borghols, M. Wagemaker, U. Lafont, E. M. Kelder, F. M. Mulder, *J. Am. Chem. Soc.* **2009**, *131* (49), 17786.

[22] L. Kavan, J. Procházka, T. M. Spitler, M. Kalbáč, M. Zukalová, T. Drezen, M. Grätzel, *J. Electrochem. Soc.* **2003**, *150*, A1000.

[23] M. Wagemaker, F. M. Mulder, *Acc. Chem. Res.* **2013**, *46*, 1206.

[24] Y. Talyosef, B. Markovsky, R. Lavi, G. Salitra, D. Aurbach, D. Kovacheva, M. Gorova, E. Zhecheva, R. Stoyanova, *J. Electrochem. Soc*. **2007**, *154*, A682.

[25] S. T. Myung, S. Komaba, N. Kumagai, H. Yashiro, H.T. Chung, T. H. Cho, *Electrochim. Acta* **2002***, 47*, 2543.

[26] N. Amdouni, K. Zaghib, F. Gendron, A. Mauger, C. M. Julien, *Ionics* **2006**, *12*, 117.

[27] D. Liu, J. Han, J. Goodenough, *J. Power Sources* **2010**, *195*, 2918.

[28] Y. Dridi Zrelli, Thèse Université Paris-Est, **2012**. Français. NNT: 2012PEST1126

[29] A. Bhatia, J. P. Pereira-Ramos, N. Emery, B. Laïk, R. I. Smith, R. Baddour-Hadjean, *ChemElectroChem* **2020**, *7*, 3420.

[30] C. Julien, F. Gendron, A. Amdouni, M. Massot, *Mater. Sci. Eng. B* **2006**, *130*, 41.

[31] B. Ammundsen, G. R. Burns, M. S. Islam, H. Kanoh, J. Roziere, *J. Phys. Chem B* **1999**, *103*, 5175.

[32] L. Boulet-Roblin, C. Villevieille, P. Borel, C. Tessier, P. Novák, M. Ben Yahia, *J. Phys. Chem. C* **2016**, *120*, 16377.

[33] W. B. White, B. A. DeAngelis, *Spectrochim. Acta A* **1967**, *23*, 985.

[34] L. Baggetto, R. R. Unocic, N. J. Dudney, G. M. Veith, *J. Power Sources* **2012**, *211*, 108.

[35] H. Xia, Y. S. Meng, L. Lu, G. Ceder, *J. Electrochem. Soc*. **2007**, *154*, A737.

[36] H. Xia, S. B. Tang, L. Lu, Y. S. Meng, G. Ceder, *Electrochim. Acta* **2007**, *52*, 2822.

[37] L. Wang, H. Li, X. Huang, E. Baudrin, *Solid State Ionics* **2011**, *193*, 32.

[38] M. Jo, Y.-K. Lee, K. M. Kim, J. Cho, J. *Electrochem. Soc.* **2010**, *157*, A841.

[39] J.-H. Kim, A. Huq, M. Chi, N. P. W. Pieczonka, E. Lee, C. A. Bridges, M. M. Tessema, A. Manthiram, K. A. Persson, B. R. Powell, *Chem. Mater*. **2014**, *26*, 4377.

[40] E. Lee, K. A. Persson, *Energy Environ. Sci*. **2012**, *5*, 6047.

[41] A. Bhatia, S. Cretu, M. Hallot, N. Folastre, M. Berthe, D. Troadec, P. Roussel, J. P. Pereira-Ramos, R. Baddour-Hadjean, C. Lethien, A. Demortière, *Small Methods* **2021**, 2100891.

[42] J. H. Xia, K. J. Kim, *Electrochim. Acta* **2014**, *137*, 169.

[43] W. H. Kan, S. Kuppan, L. Cheng, M. Doeff, J. Nanda, A. Huq, G. Chen, *Chem. Mater.* **2017**, *29*, 6818.

[44] M. Bianchini, F. Fauth, E. Suard, J. N. Leriche, C. Masquelier, L. Croguennec, *Acta Cryst B* **2015**, *71*, 688.

A. Bhatia, C. Leviel, M. Hallot, J. P. Pereira Ramos, C. Lethien*, P.Roussel*, and R. Baddour-Hadjean*

Probing the Electrochemical Li Insertion-Extraction Mechanism in Sputtered $LiNi_{0.5}Mn_{1.5}O_4$ Thin Film Cathode for Li-ion Microbattery

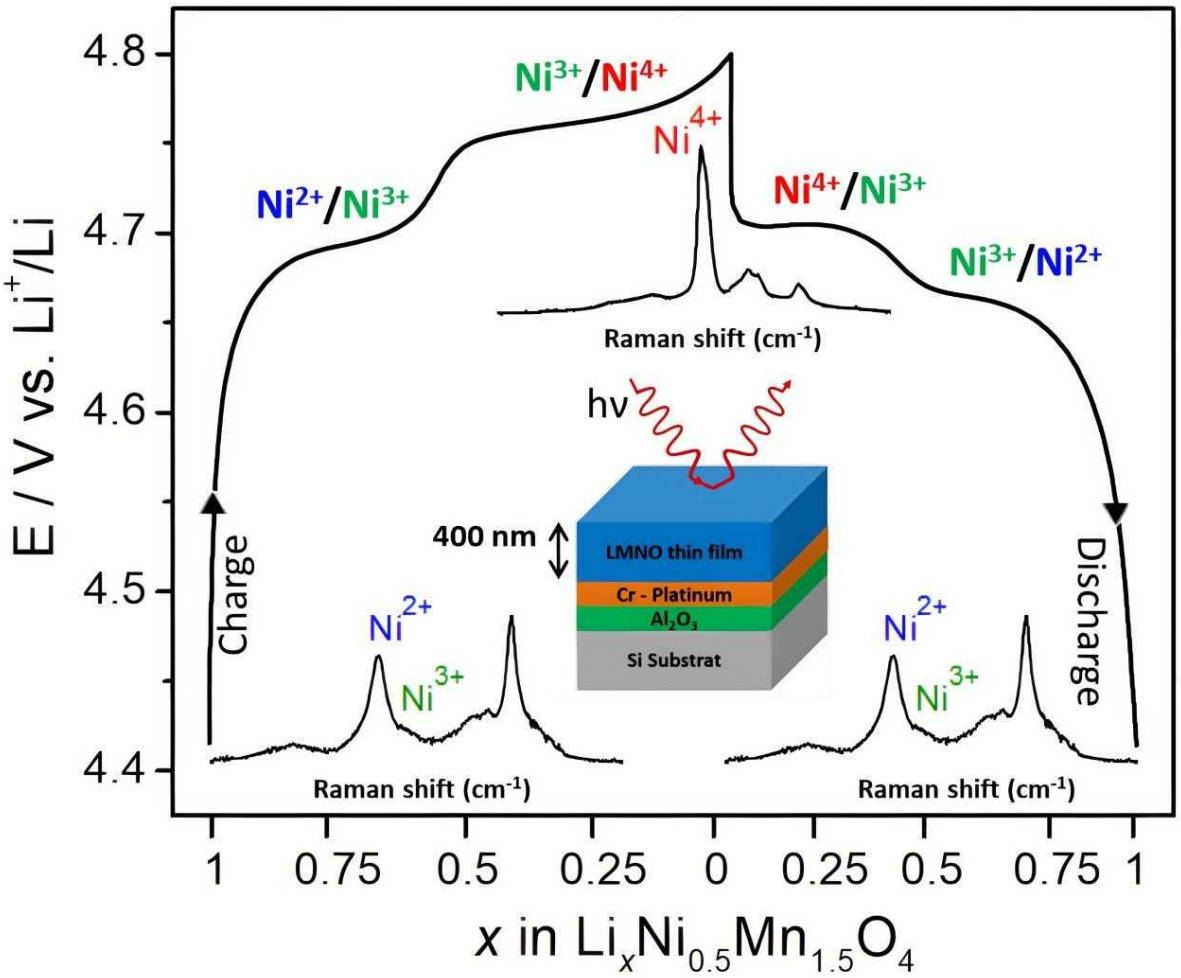

Raman spectroscopy provides a detailed and quantitative picture of changes in the Ni oxidation state in the $LiNi_{0.5}Mn_{1.5}O_4$ thin film during the first electrochemical discharge-charge cycle

Supporting Information

Probing the Electrochemical Li Insertion-Extraction Mechanism in Sputtered $LiNi_{0.5}Mn_{1.5}O_4$ Thin Film Cathode for Li-ion Microbattery

Ankush Bhatia, Clement Leviel, Maxime Hallot, Jean-Pierre Pereira Ramos, Christophe Lethien[*], *Pascal Roussel*[*] *, and Rita Baddour-Hadjean*[*]

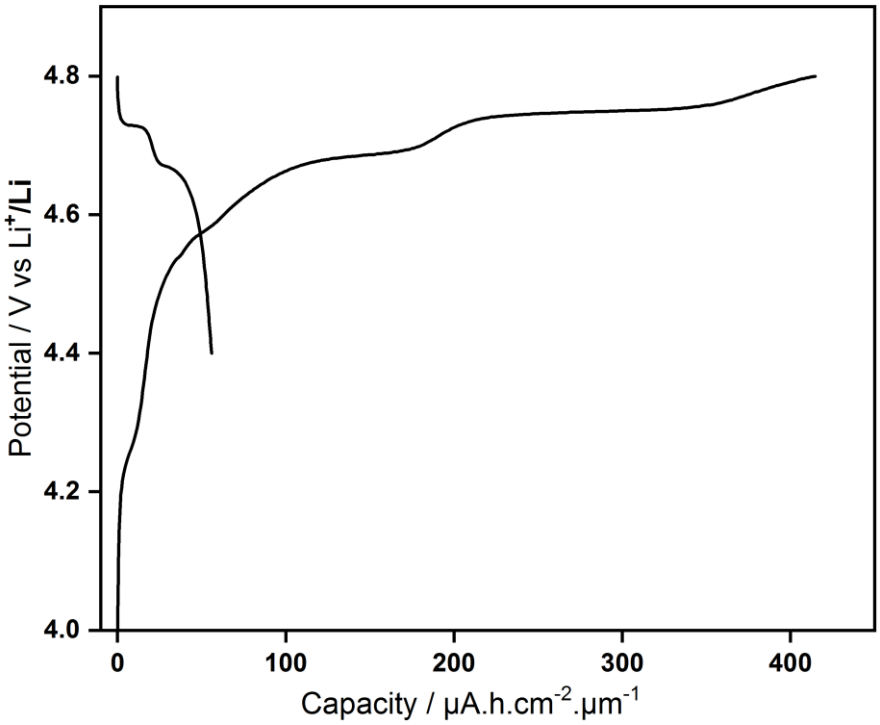

Figure S1. First charge-discharge cycle of the LNMO thin film at 1C rate**.**

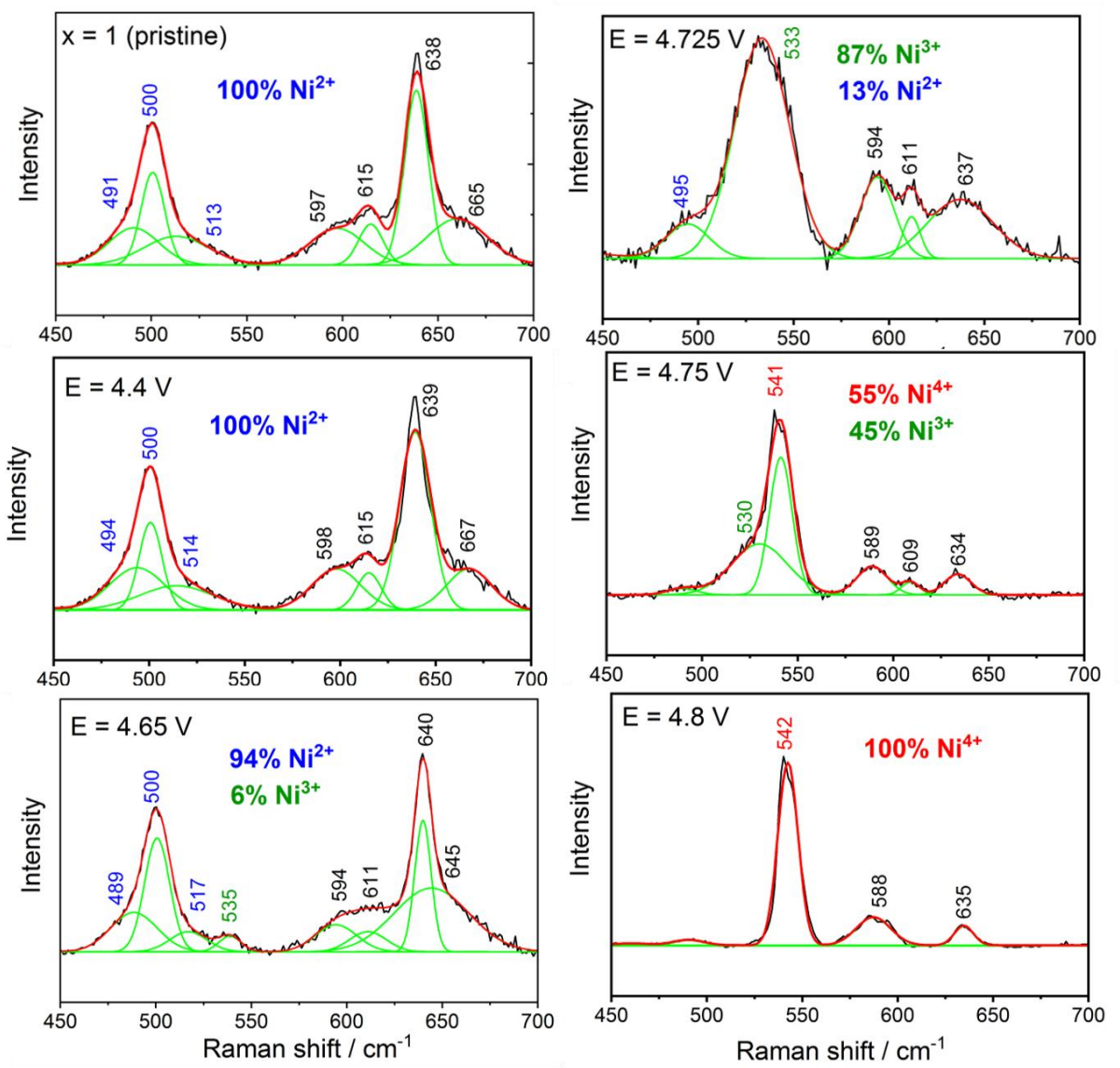

Figure S2. Raman spectra fittings during the first charge of a LNMO thin film electrode.

	Cutoff voltage (V)	x in Li_xMNO	a (Å) of Li_xMNO
CHARGE	3.3 (OCV)	0	8,1437(10)
	4.4	0.1	8,1508(7)
	4.65	0.2	8,1455(6)
	4.725	0.3	8,0918(6)
	4.75	0.4	8,0011(7)
	4.8	0.5	8,0025(9)

	x in Li_xMNO	a (Å) of Li_xMNO	a (Å) of MNO
DISCHARGE	0		8,0025(9)
	0.1	8,0650(18)	7,9992(10)
	0.2	8,0583(17)	7,9961(9)
	0.3	8,0745(5)	8,0142(9)
	0.4	8,0864(7)	
	0.5	8,1000(7)	
	0.6	8,1255(6)	
	0.7	8,1316(6)	
	0.8	8,1470(6)	
	0.9	8,1527(10)	
	1	8,1567(13)	

Table S1. Refined cubic cell parameters of the phases in presence in Li_xMNO electrodes during the charge and the discharge